Article:

S'ari, M, Blade, H, Brydson, R orcid.org/0000-0003-2003-7612 et al. (4 more authors) (2018) Towards developing a predictive approach to assessing electron beam instability during Transmission Electron Microscopy of drug molecules. Molecular Pharmaceutics, 15 (11). pp. 5114-5123. ISSN 1543-8384

https://doi.org/10.1021/acs.molpharmaceut.8b00693

Towards developing a predictive approach to assessing electron beam instability during Transmission Electron Microscopy of drug molecules

Mark S'ari †*, Helen Blade ‡, Rik Brydson †, Stephen D. Cosgrove ‡, Nicole Hondow †, Leslie P. Hughes ‡ and Andy Brown †

† School of Chemical and Process Engineering, University of Leeds, Leeds, United Kingdom

‡ Pharmaceutical Technology and Development, AstraZeneca, Macclesfield, United Kingdom

KEYWORDS: TEM, Critical fluence, Organic molecular crystal, Amorphous solid dispersion, Crystal detection

ABSTRACT: During drug development control of polymorphism, particle properties and impurities are critical to ensuring a good quality, reproducible and safe medicine. A wide variety of analytical techniques are employed in demonstrating to regulators control over the drug substance and product manufacture, storage and supply. Transmission electron microscopy (TEM) offers the opportunity to analyze in detail pharmaceutical systems at a length scale and limit of detection not readily achieved by many traditional techniques. However, the use of TEM as a characterization tool for drug development is uncommon due to possible damage caused by the electron beam. This work outlines the development of a model, using molecular descriptors, to predict the electron beam stability of active pharmaceutical ingredients (API). For a given set of conditions and a particular imaging or analytical mode, the total number of electrons per unit area which causes observable damage to a sample in the TEM can be defined as the critical fluence (C_F). Here the C_F of 20 poorly water-soluble APIs were measured using selected area electron diffraction. Principal component analysis was used to select the most influential molecular descriptors on C_F, which were shown to be descriptors involving the degree of conjugation, the number of hydrogen bond donors and acceptors and the number of rotatable bonds. These were used to generate several multiple linear regression models. The model that provided the best fit to the measured C_F data included the ratio of the number of conjugated carbons to non-conjugated carbons, the ratio of the number of hydrogen bond donors to acceptors and the ratio of the number of hydrogen bond acceptors to donors. Using this model the C_F of the majority of compounds was predicted within ±2 $e^-/Å^2$. Molecules with no hydrogen bond acceptors did not fit the model accurately possibly due to the limited sample size or the influence of other parameters not included in this model, such as intermolecular bond energies. The model presented can be used to support pharmaceutical development by quickly assessing the stability of other poorly soluble drugs in TEM. Provided that the model suggests the API is relatively stable to electron irradiation, TEM offers the prospect of determining the presence of crystalline material at low levels at length scales and limits of detection unobtainable by other techniques. This is particularly so for amorphous solid dispersions.

Introduction

Drugs classified as Class II in the Biopharmaceutical Classification System (BCS) make up more than 40% of drugs currently in development and are classed as such due to their low water solubility and high membrane permeability.[1] The bioavailability of this class of drugs is limited when dosed orally by the aqueous solubilities and dissolution rates of the active pharmaceutical ingredients (API). Different methods that physically modify the API have been implemented in order to increase its solubility and therefore enhance bioavailability. Some of which include salt formation, particle size reduction, crystal engineering of polymorphs and the production of metastable amorphous solid dispersions (ASD) consisting of a hydrophobic drug mixed within a hydrophilic matrix.[2,3] In the latter case, thermodynamic drivers always exist that can cause the metastable amorphous form to recrystallise to a more thermodynamically stable form over time or when influenced by an external stimulus, for example moisture or heat during the formulation process or storage.[4,5] If recrystallisation occurs, even in small amounts in ASD, the solubility and dissolution rate of the drug can decrease leading to lower bioavailability and further recrystallisation of the API. Standard methods for the analysis of crystallinity in ASD include powder X-ray diffraction (pXRD), Fourier transform infrared spectroscopy (FTIR) and differential scanning calorimetry (DSC). In order to assess different formulation options available during drug development, used to produce ASD, an early indication of recrystallisation is desirable and hence the need for improved limits of detection (currently 2 – 10% by volume).[6,7] This presents the opportunity to use less conventional but more sensitive techniques such as transmission electron microscopy (TEM).

TEM is an analytical technique that has very high spatial resolution and can measure crystallite size, orientation and morphological form at the single particle level and even when only trace amounts are present.[6] This is achieved through bright field (BF), dark field (DF) imaging and selected area electron diffraction (SAED). In addition energy dispersive X-ray spectroscopy (EDS) and electron energy loss spectroscopy (EELS) can provide information on elemental composition and chemical configuration. All of these techniques are well established for the characterization of metals and other inorganic materials but have been less widely applied to organic crystals, due to the ease with which these are damaged by the electron beam. Upon irradiation by TEM, secondary electrons are produced which generate free radicals and ions. These are highly reactive species that can cause bond breakage, known as radiolysis, and is thought to be the main mechanism for damage in organic crystals leading to changes in structure and, in some cases, composition and chemistry.[8-10] This damage leads to a loss of order in crystals which can be observed through the fading of diffraction spots to amorphous rings.[11,12] A loss of molecular structure can be observed in EEL spectra and possibly changes in chemical composition by EELS and EDX.[9] Mass loss of lighter atoms due to bond breakage and also sputtering may be seen as a change in mass-thickness contrast where areas that atoms have been removed appear less intense in the BF image.[9,11]

The propensity for damage to be caused to the sample by the electron beam can be quantified by measuring the characteristic/critical electron fluence (C_F) in units of $e^-/\text{Å}^2$. The terms electron dose and electron fluence tend to be used interchangeably, although strictly dose is the energy absorbed by the sample per unit mass (in units of Grays). Here we use the correct term, electron fluence and define (C_F) as the total number of electrons per unit area irradiating the sample when the intensity of a feature, such as a diffraction spot, drops to e^{-1} of the initial maximum intensity.[12] The value of the critical fluence depends on the material and a variety of experimental parameters. One of the more important parameters is the operating voltage of the microscope which affects the resolution; the amount and type of beam induced damage that occurs and the sample thickness that can produce usable data. In the case of damage by radiolysis, which is a result of inelastic scattering of electrons, an increase in accelerating voltage decreases the damage to the sample due to an inverse relationship between the inelastic scattering cross-section and accelerating voltage.[10,13,14] In general, for irradiation energies of 80 - 300 kV, biological materials have C_F in the range of 1 - 15 $e^-/\text{Å}^2$, organic crystals 0.2 - 120 $e^-/\text{Å}^2$, zeolites 100 - 600 $e^-/\text{Å}^2$, and transition metal oxides > 10^7 $e^-/\text{Å}^2$.[15-20] Organic compounds generally show a large range of C_F, making it difficult to know the electron beam sensitivity without determining it experimentally. Although it is generally believed that crystals comprised of aromatic molecules are more beam stable compared to aliphatic molecules.[21-23] Little work however has been carried out in single study on either a range of organic compounds with different structural motifs or on determining how other factors relating to molecular structure may influence C_F.

Here the C_F of 20 structurally diverse, poorly water soluble APIs was measured and correlated to molecular descriptors, obtained from the 2D chemical structure. Principal component analysis (PCA) was used to provide insight into which molecular descriptors had the highest influence on C_F for this set of compounds. A simple model was generated to correlate the measured C_F with the most significant molecular descriptors obtained from the PCA.

The predictive model could allow compounds of interested to be screened by their chemical structure for their suitability for TEM analysis; minimizing experimental time. TEM can identify trace amounts of crystalline material and provide more detailed analysis of crystalline regions which are crucial in the development of amorphous solid dispersions.

Materials and Methods

Materials

The majority of APIs used in this study were selected based on work by Nurzynska et al., where a database of 1327 APIs was reduced to 171 by filtering compounds that had poor aqueous solubility (log S_w < -4), low molecular weight (M_w < 800 g/mol) and were neutral (uncharged in the gastrointestinal pH range 1.2 - 6.5).[24] After filtering, PCA was used to categorize the remaining APIs into 35 different groups, each containing between 1 - 50 compounds, with similar chemical structures. From these groups 25 compounds were selected to be representative of the larger population. From this 19 were selected for this work, with the other 6 being unavailable. Indomethacin, another poorly water soluble compound, was also included to give a total of 20 different APIs. All samples were kindly supplied by AstraZeneca. The chosen compounds are listed in Table 1 of the supplementary material together with their chemical structures.

TEM Methodology

The crystalline APIs (crystal references shown in Supplementary material) were prepared for TEM by grinding the powder and dispersing in water. By suspending the powder in water this would prevent it from readily dissolving and any changes to the crystal form occurring. Approximately 3 - 4 drops of the suspended powder was placed onto a 400 mesh continuous carbon coated copper grid. The samples were examined in a Tecnai F20 TEM/STEM operated at an accelerating voltage of 200 kV, equipped with a field emission gun using an extraction voltage of 4.5 kV. The images were captured using a Gatan Orius CCD camera. The electron flux (J), which is the rate of electrons passing through the sample per unit area, was controlled by altering the C1 condenser lens by selecting different spot sizes, generally between 7 and 9, and by defocusing the C2 condenser lens to lower the intensity of the electron beam. Selected area electron diffraction patterns were acquired using an aperture size of 1.1 µm at the image plane from crystal areas that appeared relatively thin. In some cases the crystals were fairly large

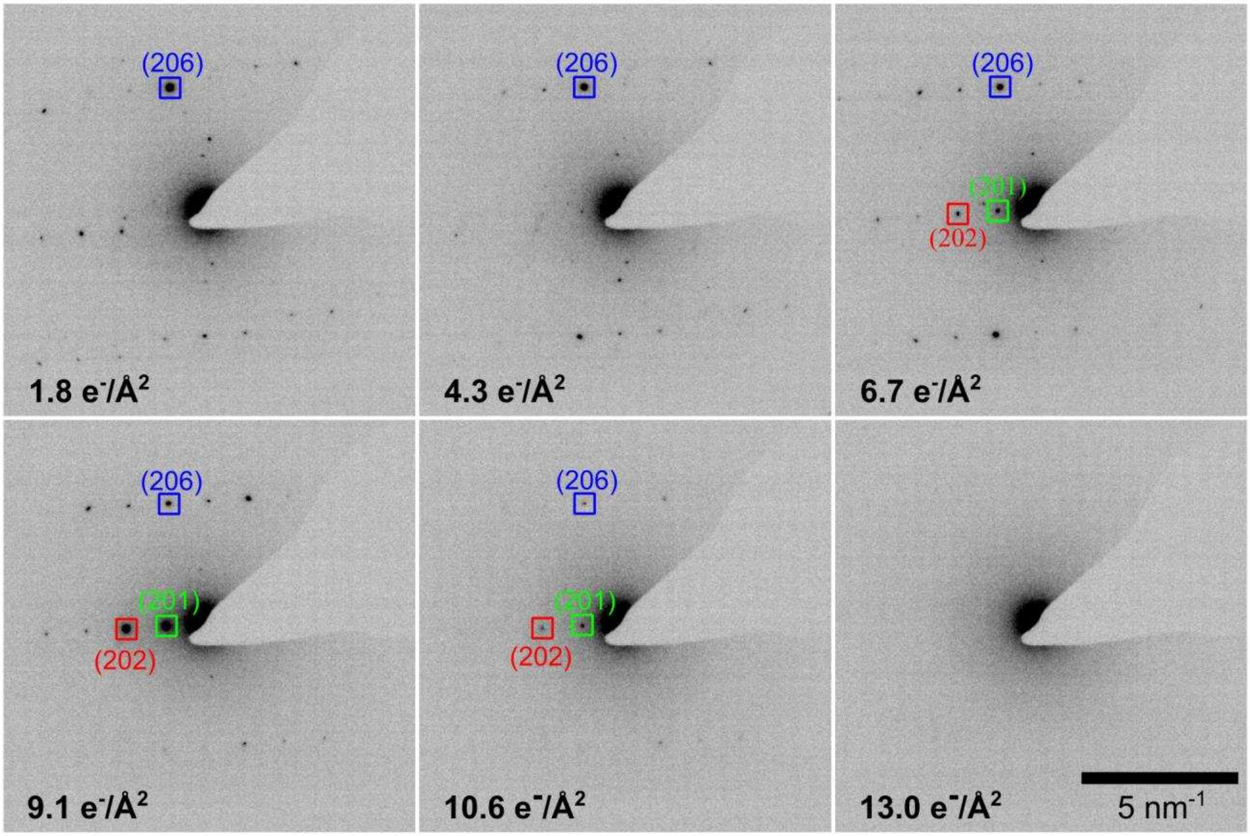

Figure 1. Example of an electron diffraction pattern time series of griseofulvin, acquired using an electron flux of 0.02 e$^-$/Å^2 s. In the images the (206) reflection gradually reduces in intensity as the electron fluence accumulates until it completely disappears, indicating loss of crystallinity. The cumulative electron fluence for each image is shown in the bottom left. See results and discussion section for more in depth discussion on the other reflections.

(0.5 - 2 μm) and thick allowing very few electrons to pass through the samples, these areas were mostly avoided when acquiring SAED patterns. The exact size and thickness of crystals varied depending on the sample.

All of the crystals were randomly orientated, sometimes with several crystals sitting above or below each other. Successive SAED patterns were collected at ~ 15 - 30 second intervals until no diffraction spots were visible (Figure 1) and the time between the initial exposure and collection of the first diffraction pattern was also recorded.

It was assumed that the damage occurring within the sample was due to the accumulated fluence and was independent to J. This has been shown to be true for organic compounds when low values of J (<0.2 e-/Å^2 s) are used.[23] An electron flux between 0.01 – 0.03 e-/Å^2 s was used for the experiments and calculated using equation 1. This equation estimates the probe current using a calibration curve provide by the microscope manufacture (FEI, now ThermoFisher Scientific) based on the measured brightness (i.e. exposure time) incident onto the fluorescent screen. The electron flux is then calculated by multiplying by the electron beam area.

$$J\ (e^-/\text{Å}^2\ s) = \frac{a\ \times b\ \times \varepsilon}{T_e\ \times\ C_s\ \times e} \times \frac{M^2\ \times\ 10^{-20}}{\pi\ \times r^2} \qquad (1)$$

where a is a calibration constant (1.875 x 10^{-15}), b is a constant relating to the accelerating voltage (1.3 at 200 kV), ε is the emulsion setting which relates to the sensitivity of the TEM's phosphor viewing screen (equal to 2 during TEM operation), C_s is the screen correction factor specific to the phosphor screen used in the microscope (in this case equal to 1.2) and e is the elementary charge of an electron (1.6 x 10^{-19} C). The exposure time (T_e) can be read from the exposure meter on the TEM phosphor screen and is dependent on the C1 and C2 condenser excitation, the source extraction voltage and size of the condenser aperture. To acquire the most accurate reading of the screen current the beam must be within the diameter of the screen with no sample in the field of view and no objective aperture inserted. M is the magnification at the viewing screen and r is the radius of the electron beam on the screen, in meters, and is controlled using the C2 condenser lens. It should be noted that while beam current estimates from the phosphor screen provide a good approximation of the electron flux the use of a Faraday cup provides a more accurate measurement and should be used when available.

A minimum of five electron diffraction time series were taken for each compound, resulting in an average of ~80 diffraction spots per compound, however in some samples it was only possible to obtain 8 - 30 spots, while in others, where more than five series were taken, over 150 spots were analyzed.

TEM Data Analysis

Electron diffraction patterns were analyzed using custom made MatLab scripts, which measured the intensity (I) of all diffraction spots and d-spacings for a particular electron fluence (F) calculated using equation 2.

$$F\ (e^{-}/\text{Å}^2) = J \times (t_0 + t) \quad (2)$$

where t_o is the time between the area first being exposed to the electron beam and the time taken to record the first diffraction pattern and t is the subsequent exposure time, both in seconds.

All intensities were normalized (I/I_{max}) to the maximum intensity for that particular diffraction spot. Critical fluence was then calculated by plotting the electron diffraction spot decay curves of $\ln(I/I_{max})$ against F and fitting a linear function to approximate where I/I_{max} drops to e^{-1} (or -1 for $\ln(I/I_{max})$).

Principal Component Analysis

Different molecular descriptors that may influence C_F were used as input parameters for PCA, shown in Table 1. Hydrogen bond donors were defined as N, O, S atoms covalently bonded to at least one hydrogen atom and hydrogen bond acceptors were defined as N, O, S and halogen atoms with at least one lone pair. Rotatable bonds were considered as any single bonds not within a ring bound to any non-terminal heavy atom and conjugated carbons were taken to be any sp^2 hybridized carbon atom. Values for each molecular descriptor for each compound are shown in the supplementary material. The selection of parameters used was based on readily obtainable values from the chemical structure and ones that have been shown previously to increase C_F.[18,26,27] Before PCA was performed the data were pre-processed by scaling the input parameters to have unit variance using the "*pca*" function in MatLab.

Multiple Linear Regression

Multiple linear regression (MLR) was used to quantify the relationship between several predictor variables and a dependent variable, providing an equation that could be used to predict C_F. A multiple linear regression model can be represented as:

$$y = \beta_0 + \beta_1 x_1 + \beta_2 x_2 + \cdots + \beta_k x_k \quad (3)$$

where k is the number of predictor variables, β_o is a constant, β_1, β_2, …, β_k are the regression coefficients and y is the dependent variable (C_F). The parameters that were shown to have an influence on C_F during PCA were used as the predictor variables to create a number of MLR models. In order to select the best and simplest model without over fitting, MLR was carried out using the "*steplm*" function in MatLab, this function adds or removes variables to increase or decrease the value of certain selection criteria, these being: adjusted R^2, Bayesian Information Criterion (BIC) and Akaike Selection Criterion (AIC).[28,29] The adjusted R^2 value is a statistical diagnostic tool used to determine the percentage of the variability of the dependent variable explained by the variation of the independent variables and takes into account the number of variables in the model. A larger adjusted R^2 suggests that the model provides a better fit. AIC and BIC are both information criteria which are used to measure goodness of fit, by calculating the difference between a given model and the "true" underlying model. The difference between AIC and BIC is how additional parameters that are included in the model are penalized. Smaller values calculated by AIC and BIC indicate that a model is closer to the "true" model; therefore a smaller value suggests a more accurate model. By using these selection criteria, the stepwise regression method can add or remove variables in order to improve the model over that expected by random chance.

Table 1. Input parameters used in principal component analysis. The parameters highlighted in bold were shown to be correlated to critical fluence in this work.

Parameter	Meaning
T_m	Melting temperature
M_w	Molecular weight
HB_d	Number of hydrogen bond donors
HB_a	Number of hydrogen bond acceptors
rotB	Number of rotatable bonds
$Ring_{arom}$	Number of aromatic rings
$Ring_{aliph}$	Number of aliphatic rings
nX	Number of halogen atoms
C_c	Number of conjugated carbons
C_{nc}	Number of non-conjugated carbons
C_t	Total number of carbons
$Atom_{nH}$	Number of non-hydrogens
$Atom_H$	Total number of hydrogens
$HB_{d:a}$	Number of hydrogen bond donor/acceptor ratio
$HB_{a:d}$	Number of hydrogen bond acceptor/donor ratio
$C_{c:nc}$	Number of conjugated/non-conjugated carbon ratio
$C_{c:ct}$	Number of conjugated/total carbons ratio
$C_{nc:ct}$	Number of non-conjugated/total carbons ratio
$Atom_{nH:H}$	Number of non-hydrogens to hydrogen ratio
C_F	Critical fluence

Results and Discussion

Critical Fluence Measurements

As mentioned earlier this is used to calculate the C_F which it should be noted varies by < 0.1 when adding or removing any datum point on any of the plots (generally adjusted R^2 shifts by ~0.01-0.03 in these circumstances). In Figure 2a the intensity is at its maximum within the first two data points, corresponding to an electron fluence of <2 $e^-/Å^2$. The intensity then decays and can be approximated to a linear function until $\ln(I/I_{max})$ is equal to -1.5 (22% of the maximum intensity). At this point the diffraction spot is below e^{-1} of the maximum intensity and the C_F can be calculated from the linear function. The spot continues to decrease in intensity until around 10 $e^-/Å^2$ where the intensity plateaus and becomes similar to the background level, no longer visible in the electron diffraction pattern. Previous studies have observed similar decay profiles in other materials.[18,27,30–34] Similar profile shapes were seen for the majority of diffraction spots from each sample. In the intensity of the first few data points small fluctuations could be seen, where there was an initial increase in intensity before the decay. This may be attributed to a rapid loss of mass upon irradiation, reorientation or conformational changes occurring in the sample, producing a structure that is more stable to the electron beam.[8,27,35,36] Decreases in intensity are due to damage of both the chemical and crystal structure and in most cases it appears that both occur simultaneously.[8] However, it has been demonstrated in phthalocyanines that the crystal structure is lost before the chemical structure while studies on tetracene show that the chemical structure is destroyed first.[8]

In Figure 2b the decay profile exhibits an initial plateau, between an electron fluence of 0 - 6 $e^-/Å^2$, here the spot intensity remains above 90% of the maximum before following a linear decay, at an electron fluence >9 $e^-/Å^2$, similar to the one shown in Figure 2a but at an increased rate. This plateau is unexpected at room temperature and, as well as being observed for griseofulvin (5.78 Å) was also observed in other compounds: dutasteride (3.31 Å and 6.62 Å) and in six different spacings in tolnaftate (3.07 Å, 3.33 Å, 3.43 Å, 3.97 Å, 4.15 Å and 5.25 Å). Such a plateau has been referred to as latent decay by Siegel and Wade and is typically observed in samples that are studied at cryogenic temperatures.[37,38] A proposed explanation for this decay profile was put forward by Siegel; the diffusion rate of damaged fragments decreases at low temperatures, preventing a change in the crystalline order.[38] Once the number of fragments reaches a critical concentration, the fragments are able to diffuse away, no longer preventing changes to the structure and hence decreasing order at the corresponding diffraction intensities.[30,31,37] The reason for a similar decay profile being apparent at room temperature is not clear but it may be caused by steric hindrance preventing fragments from diffusing. The occurrence of a thermally activated reverse reaction or a healing effect may prevent a proportion of the damage. Allowing for the structure to stay intact until the cumulative damage is too great and the structure finally breaks down. In Figure 2c, the decay profile starts with the diffraction spots at low intensities and as the fluence increases the intensity initially increases. At ~8 $e^-/Å^2$ the spot is at its maximum brightness and there is then a rapid decay in intensity levels. This has been referred to as the enhanced intensity effect and thought to occur in relatively thin samples (<100 nm) with a high density of lattice defects.[31,32,37] Some defects may be present before electron beam exposure but the majority of lattice defects i.e. point defects are likely to be caused during irradiation.[8] When there is a high density of lattice defects electrons that pass through the sample encounter strain fields causing the intensity of the beam to increase; leading to the enhanced intensity seen in the electron diffraction pattern.[39,40] In addition, reconfiguration or orientation into a more stable structure via the production of radiation induced derivatives or mechanical movement of the crystal causing it to tilt off the original axis and can increase the relative intensities.[32] Seemingly random and erratic changes in intensity have also been seen in other studies where there are multiple peaks in the decay curves and are thought to occur in relatively thick samples (multiple hundreds of nm). The decay profiles of these samples have been shown to follow the movement of bend contours in bright field TEM images.[37] This is due to a combination of mechanical movement and structural changes within the crystal altering the lattice orientation relative to the electron beam.[31,35,37,38]

Due to the limited amount of time available before damage occurred in the current materials it was not possible to tilt a particular crystalline particle onto a recognizable zone axis. This means the crystals were randomly orientated and the majority of diffraction patterns showed different inter-planar spacings making it difficult to provide a representative C_F for a particular inter-planar spacing. Most previous studies examined thin crystals with preferred orientations which provide easily comparable diffraction pattern series via selection of a single first order diffraction spots in order to calculate C_F.[17,18,30,31,37] Instead of selecting one spot to provide a measurement for C_F, in this work an average of all the spots measured was taken to give an overall measurement of C_F, hence crystallinity will be assessed in random orientations (Table 2). This average includes higher order spacings that are not generally included in C_F measurements. It is observed that diffraction spots with smaller d-spacings generally fade faster, corresponding to a loss of high resolution information and short range order, while the general molecular packing and long range order (large d-spacings) remain intact even though the molecules are fragmenting and losing their short range order.[41] Including the smaller d-spacings within the average C_F measurement generally provides a smaller value of C_F, shown in Table 2, where the diffraction spots have been grouped into d-spacing ranges (<2 Å, 2 – 4 Å, 4 – 6 Å and >6 Å). The majority of samples follow the trend of smaller spacings corresponding to smaller values of C_F, however for griseofulvin the spacings >6 Å have a lower average C_F compared to the spacings within the range 4 – 6 Å; there is also a larger spread of measured fluence as can be seen from the standard deviation. This may be a result of preferential

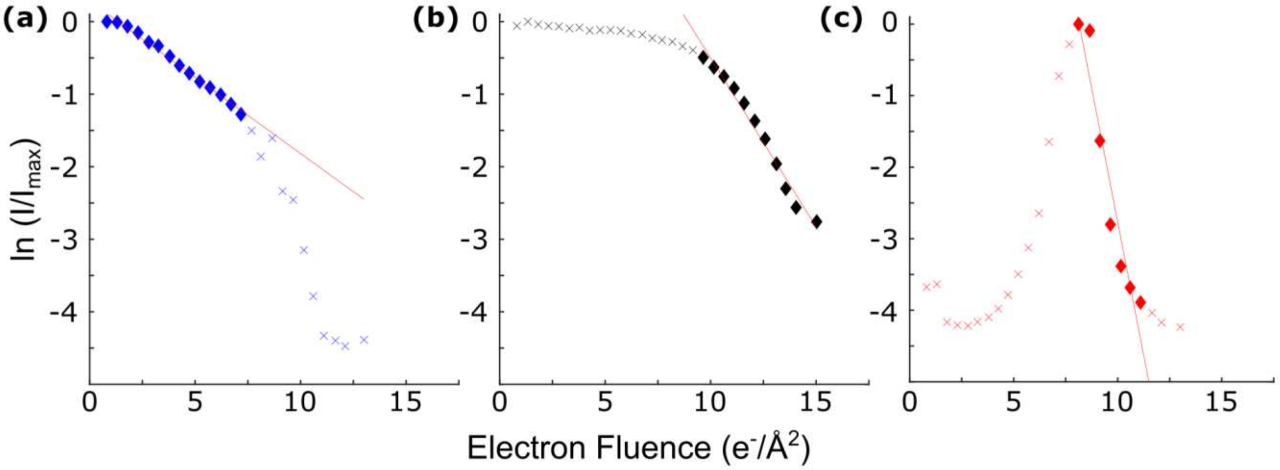

Figure 2. Intensity curves of griseofulvin that demonstrate the different decay profiles observed, the linear sections of each graph are fitted using a straight line to calculate C_F (a) Linear decay of 2.35 Å spacing, equal to a (206) reflection (b) Latent decay of 5.78 Å spacing, equal to a (111) reflection (c) Enhanced intensity effect followed by linear decay of the 4.10 Å spacing, equal to a (202) reflection.

Table 2. Mean critical fluence and standard deviation of each compound calculated from diffraction pattern data. Critical fluence when all measured diffraction spots are included are shown and the number of spots used in these averages. Columns 2, 3, 4 and 5 separate the diffraction spots based on d-spacing and show the calculated values when only spots within those chosen ranges are included in the average. All units are in e$^-$/Å^2.

API	d < 2 Å	2 – 4 Å	4 – 6 Å	d > 6 Å	All d-spacings	Total number of spots average
Amcinonide	1.0 ± 0.1	1.1 ± 0.2	1.4 ± 0.3	1.5 ± 0.4	1.3 ± 0.3	42
Bicalutamide	1.6 ± 0.2	2.9 ± 0.7	3.1 ± 0.6	4.4[1]	2.9 ± 0.8	51
Celecoxib	3.8 ± 1.4	5.2 ± 1.2	5.8 ± 0.7	6.0 ± 3.4	4.5 ± 1.6	161
Ciclesonide	-	-	0.6 ± 0.1	0.7 ± 0.1	0.6 ± 0.1	8
Cilostazol	1.6 ± 0.5	2.1 ± 0.9	2.5 ± 0.9	3.7[1]	2.1 ± 0.9	166
Drospirenene	0.8 ± 0.3	0.9 ± 0.3	0.9 ± 0.3	1.2 ± 0.3	0.9 ± 0.3	105
Dutasteride	1.9 ± 0.4	2.1 ± 0.4	2.5 ± 0.6	2.7 ± 0.4	2.2 ± 0.5	70
Efavirenz	-	0.5 ± 0.1	0.4 ± 0.1	0.9 ± 0.1	0.5 ± 0.1	25
Felodipine	1.8 ± 0.7	2.1 ± 0.9	2.7 ± 1.2	2.0 ± 0.3	2.1 ± 0.9	67
Griseofulvin	4.4 ± 2.2	5.8 ± 3.1	7.6 ± 3.6	6.1 ± 3.4	5.3 ± 2.9	111
Indapamide	2.7 ± 1.0	4.8 ± 1.9	5.0 ± 2.0	6.1 ± 2.2	4.5 ± 2.0	103
Indomethacin	2.8 ± 1.6	2.8 ± 2.0	2.8 ± 2.4	3.9 ± 2.7	2.9 ± 1.9	241
Lopinavir	-	0.5 ± 0.1	0.7 ± 0.3	0.5 ± 0.1	0.6 ± 0.2	25
Nandrolone	1.3 ± 0.2	1.4 ± 0.3	1.5 ± 0.2	1.3[1]	1.4 ± 0.2	85
Nifedipine	0.7 ± 0.1	0.7 ± 0.2	0.7 ± 0.3	0.9 ± 0.1	0.7 ± 0.2	60
Nimodipine	2.1 ± 0.8	3.0 ± 0.7	2.7 ± 0.9	-	2.7 ± 0.8	65
Nisoldipine	-	0.3 ± 0.1	0.2 ± 0.0	-	0.3 ± 0.1	14
Probucol	0.1 ± 0.1	0.1 ± 0.0	0.2 ± 0.1	0.1 ± 0.0	0.1 ± 0.1	61
Simvastatin	0.6 ± 0.2	0.7 ± 0.2	0.7 ± 0.2	-	0.7 ± 0.2	45
Tolnaftate	8.4 ± 4.6	13.8 ± 4.7	15.2 ± 3.8	14.6 ± 1.7	13.0 ± 5.1	165

[1] Only data from one diffraction spot available.

damage along certain crystal planes, causing the intensity of these spots to fade irrespective of their inter-planar spacing. The large standard deviation may also be a result of sample thickness which was not taken into consideration during this study due to the difficulties associated with measuring this powder samples. Thickness has been shown to give a linear dependency to the C_F of the sample, with thicker samples providing larger C_F values; as a result of heating and other effects.[9,42]

The detection of diffraction spots may be improved through the use of an imaging filter and the latest generation of electron detectors; both of which may affect the observed intensity decay and lengthen the life of the crystal relative to the background signal. In the former case the imaging filter can eliminate or significantly reduce the effects of inelastic scattering, which is particularly problematic for low Z materials such as these pharmaceuticals and has previously been used to remove the effects of inelastic scattering in 2D proteins crystals.[43] In the latter case improvements in the detector quantum efficiency will increase the signal-to-background ratio allowing easier identification of diffraction spots at low electron fluence.

Principal Component Analysis (PCA)

Using the molecular descriptors from Table 1 and the experimentally determined C_F, PCA was carried out to discover if a correlation exists between these descriptors and C_F. The results showed that 86% of the total variance in the input parameters could be explained using four principal components (PC), where 40%, 24%, 14% and 8% of the variance is explained by PC1, PC2, PC3 and PC4 respectively (shown by the scree plot in the supplementary material). The PC loadings were then used to find a correlation between each molecular descriptor and C_F. This was achieved by plotting PC loadings against each other and measuring the component angle between C_F and each molecular descriptor. The graphs and an example of one of the component angles being measured can be seen in Figures 3a and 3b. A value of cos $\theta \sim 1$ suggests that the molecular descriptor influences C_F positively, if cos $\theta \sim -1$ it suggests a negative correlation and if cos $\theta \sim 0$ then the molecular descriptor is independent of C_F. For there to be an overall correlation between the molecular descriptor and C_F the sample relationship must hold true in both PC1 vs PC2 (θ_{PC1-2}) and PC3 vs PC4 (θ_{PC3-4}). The graph of θ_{PC3-4} against θ_{PC1-2} in Figure 3c shows clearly the descriptors that are positively correlated, negatively correlated and independent when considering all four PCs.

From the 19 molecular descriptors entered into the PCA, 9 were shown to be either positively or negatively correlated to C_F, these being the number of hydrogen bond donors (HB_d), the number of hydrogen bond acceptors (HB_a), the number of rotatable bonds (rotB), the number of aromatic rings ($Ring_{arom}$), the number of conjugated carbons (C_c) and the ratio of number of hydrogen bond donors to acceptors ($HB_{d:a}$), the ratio of number of hydrogen bond acceptors to donors ($HB_{a:d}$), the ratio of number of conjugated to non-conjugated carbons ($C_{c:nc}$) and the ratio of number of conjugated carbons to total number of carbons ($C_{c:t}$). It should be noted that using the C_F for different d-spacing ranges, as opposed to the overall average, gave little or no difference to the results, and thus the results presented in Figure 3 are from the overall averages.

The molecular descriptors which gave a positive correlation to C_F were $Ring_{arom}$, C_c, $C_{c:nc}$ and $C_{c:t}$. It was expected that the number of aromatic rings would give a positive correlation since previous studies have suggested that the delocalization of electrons in a ring allows the energy deposited from the electron beam to be shared and dissipated more effectively which then decreases the formation of damaging radicals.[22,23,26,33] The presence of benzene rings have been suggested to influence the delocalization of electrons up to twelve atoms away from the ring.[21]

The molecular descriptors which gave a negative correlation to C_F were HB_d, HB_a, rotB, $HB_{d:a}$, $HB_{a:d}$. The number of rotatable bonds relates to the number of different structural configurations the molecules can undertake and in this study the greater number of rotB lead to a lower C_F. Surprisingly factors that related to hydrogen bond donors/acceptors all appeared to give a negative correlation to C_F. This was initially unexpected since organic crystals are held together by weak intermolecular forces such as van der Waals bonding, hydrogen bonding and π-π stacking of aromatic rings and it was assumed that if more hydrogen bonds were present then the crystal would be more stable i.e. requiring a higher electron fluence before damage occurred. If a crystal is mainly stabilized through hydrogen bonding removal of the hydrogen bonded atoms by the electron beam may cause disruption to the crystal structure at an increased rate as compared to structures that are mainly stabilized through van der Waals or π-π stacking. The hydrogen atoms may be removed via knock on damage, where the electron collides with the hydrogen atom directly and due to the low binding energy the atom is removed from the structure.[11]

However, no correlation between the overall number of hydrogen atoms and C_F was found. Alternatively the hydrogen atoms may be removed through radiolysis where the covalent bond between the hydrogen atom and another atom (C-H, O-H, N-H etc.) is broken and due to the size of the hydrogen atom it can diffuse away preventing reformation of the covalent bond.[8] When hydrogen bonding is present the adjacent covalent bond is weakened making it more susceptible to damage by radiolysis.[40] The weakening of the adjacent covalent bond was demonstrated in a study by Conroy et. al. using liquid cell TEM where the mineral boehmite (γ-AlOOH), a layered material that is structurally stabilized through hydrogen bonds, was exposed to electron irradiation and layers of the material were found to delaminate and dissolve.[44] In comparison a similar mineral, gibbsite (γ-Al(OH)$_3$), showed no delamination or dissolution suggesting that in boehmite the hydrogen bonding network breaks down. Further evidence supporting the weakening of adjacent

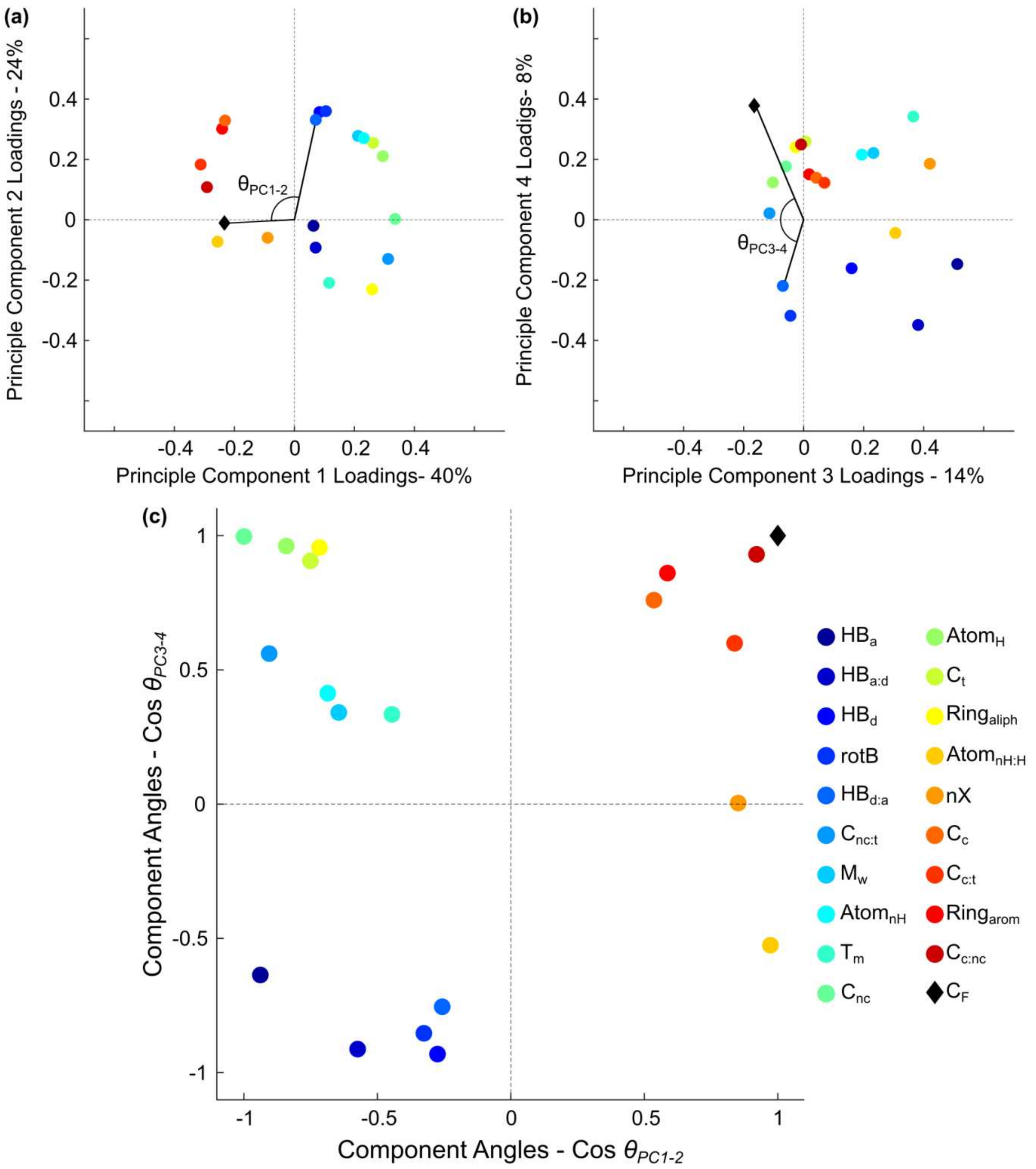

Figure 3. (a) PCA loadings for principal component 1 and 2 (b) PCA loadings for principal component 3 and 4 (c) Angles between critical fluence and other molecular descriptors calculated from graphs a and b. Points in the top right quadrant are positively correlated in all principal components, points in the bottom left quadrant are negatively correlated in all principal components and all the other molecular descriptors are independent of critical fluence (which we demonstrate here correlates to itself, as expect.

covalent bonds comes from gamma irradiation experiments that showed significantly more hydrogen was released for boehmite as compared to gibbsite.[45] This was also consistent with corresponding measurements of O-H stretch frequencies in IR spectroscopy, which indicated that the O-H bonds strength was weaker (i.e. lower wavenumber) in boehmite (3290 - 3085 cm^{-1}) compared to gibbsite (3463 - 3468 cm^{-1}), but the hydrogen bonding between structural units was stronger.[46,47] This effectively implies that strong hydrogen bonding between molecular units weakens the neighboring covalent bond (O-H, N-H etc.) making it more susceptible to radiolysis and break down of the structure leading to a negative correlation with the C_F. This could in principle be correlated to C_F for compounds in this study by measuring the O-H and N-H bond strength of each compound by IR spectroscopy.

Melting temperature (T_m) which had previously been shown to be correlated to the C_F for polymers was not correlated to C_F for these 20 compounds.[18] Previously, significant deviations for conjugated systems were observed when comparing C_F to T_m due to the fact that conjugated systems have little effect on increasing the T_m directly (which is related to the flexibility and mobility of a molecule), whereas conjugation increases the radiation resistance of a molecule.[18,41]

The majority of samples measured here contained at least one conjugated ring possibly explaining why this set of data did not follow the same trend. The number of halogens (nX) has also been previously shown to increase C_F; in the study by Clark et al. all hydrogens in copper phthalocyanine were substituted by F or Cl and the halogenated compounds showed increases in C_F.[27] The substitution was thought to create a caging effect where the F and Cl atoms, due to their much larger size compared to hydrogen, sterically hindered the diffusion of molecules preventing/delaying radiation damage. Here no correlation was found between nX and C_F, possibly because the compounds that possessed either F or Cl (amcinonide, bicalutamide, celecoxib, dutasteride, efavirenz, felodipine, griseofulvin, indapamide and indomethacin) contained very few of these (between 1 and 6) compared to the number of hydrogens (9 - 35).

Multiple Linear Regression (MLR)

From the molecular descriptors shown to be correlated to the C_F, several multiple linear regression models were constructed using stepwise regression and judged based on the selection criteria mentioned earlier. This was done to generate potential models that would then be tested further to give the best prediction for C_F. For each criterion 20 different models were generated where one sample was excluded at each iteration. By excluding one sample during the iteration process the best derived model equation sometimes changed, due to fitting a slightly different dataset.

The models that were derived more than once are shown in Table 3. To find which of these gave the best fit for C_F; further models were generated using the "*fitlm*" function in MatLab with the "RobustOpts" turned on, in order to reduce the effects of extreme data points such as tolnaftate which has a C_F more than twice as large as the next highest compound. The root mean squared error (RMSE) and adjusted R^2 was then used to judge which of these models gave the best prediction for C_F. Out of all the potential models generated model 1 occurred most frequently and gave the best fit (adjusted R^2 0.49) alongside one of the smallest error values (RMSE 2.35). Three predictor variables are used in this model all of which are ratios; hydrogen bond donors to acceptors, hydrogen bond acceptors to donors and conjugated carbons to non-conjugated carbons. Model 2 included rotB in addition to $C_{c:nc}$, $HB_{d:a}$ and $HB_{a:d}$. This gave a similar RMSE value to model 1 but decreased the adjusted R^2 value indicating a worse fit. $C_{c:nc}$ or C_c appeared in every equation suggesting it is important to include information on conjugation when predicting C_F, although $C_{c:nc}$ did not provide an adequate prediction on its own, as shown in model 4 which had the highest RMSE (3.00) and lowest adjusted R^2 (0.28). Model 6 included a total of 5 predictor variables and had a higher RMSE and lower adjusted R^2 than models 1 and 2 which suggests that adding too many variables decreases the effectiveness of the model and that a sufficiently good prediction for C_F can be achieved using the predictor variables in model 1. The plot of predicted C_F against the experimental C_F using the equation for model 1 is shown in Figure 4a.

Table 3. MLR equations to predict C_F for the most commonly generated models through stepwise regression when excluding one sample on each iteration. The MLR coefficients shown are averaged across all iterations. The mean squared error and adjusted R^2 show how well each model compares.

Model	Equation	RMSE	Adjusted R^2	Frequency
1	$3.20 - 3.19\ HB_{d:a} - 0.27\ HB_{a:d} + 0.47\ C_{c:nc}$	1.91	0.47	36
2	$3.11 + 0.03\ rotB - 3.51\ HB_{d:a} - 0.28\ HB_{a:d} + 0.49\ C_{c:nc}$	1.89	0.44	12
3	$3.09 + 0.14\ C_c - 4.14\ HB_{d:a} - 0.26\ HB_{a:d}$	2.08	0.37	2
4	$1.08 + 0.50\ C_{c:nc}$	2.38	0.29	2
5	$2.15 - 0.34\ HB_d - 0.13\ HB_{a:d} + 0.48\ C_{c:nc}$	2.14	0.34	2
6	$0.32 - 1.58\ HB_d + 0.69\ HB_a + 3.90\ HB_{d:a} - 0.46\ HB_{a:d} + 0.53\ C_{c:nc}$	2.04	0.32	2

The three compounds that showed the highest error in predicted C_F (Figure 4b) all contain no hydrogen bond donors, with tolnaftate having an experimental C_F of 16.3 $e^-/\text{Å}^2$ whilst being predicted at 7.5 $e^-/\text{Å}^2$. The relatively high electron beam stability of tolnaftate compared to other compounds may be due to a lack of hydrogen bonds and the presence of two fused benzene rings, only seen in tolnaftate, promoting largescale charge and heat delocalization across the whole molecule. The work presented

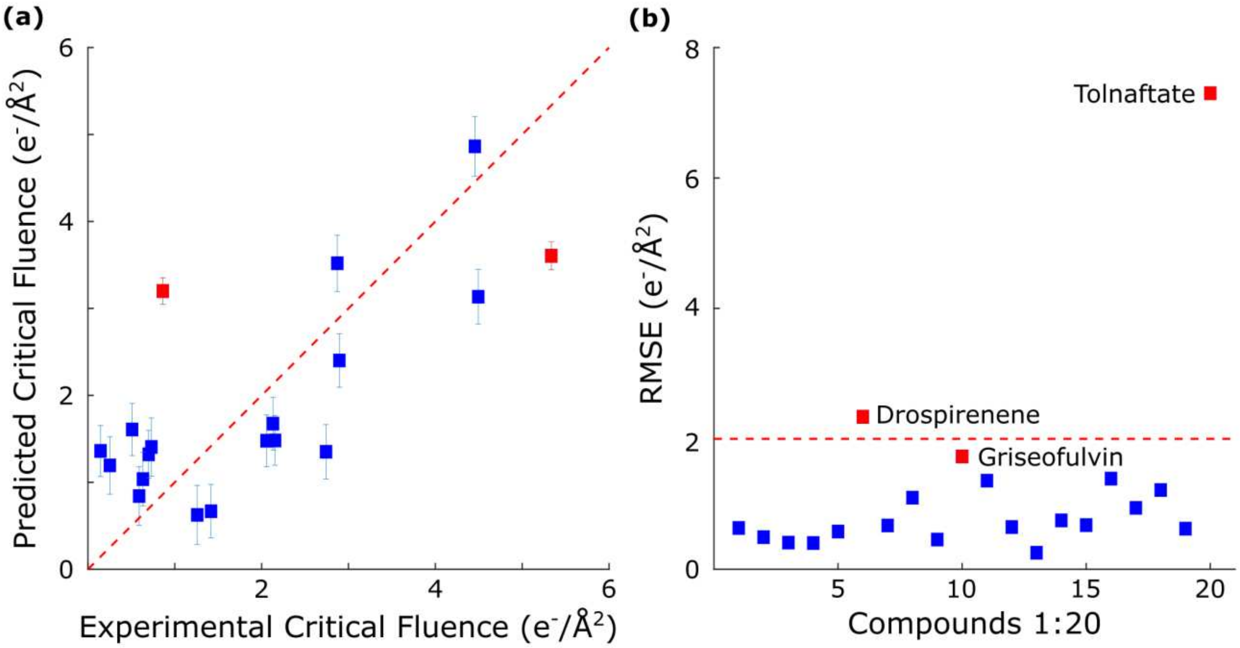

Figure 4. (a) Predicted C_F of each compound, calculated using the regression equation in model 1 vs experimental C_F. The error bars represent the standard error of the mean and points shown in red are two of the compounds that are poorly predicted. The data point for tolnaftate is not shown on the graph as the experimental C_F is twice as large as the next highest compound. The red line is for y = x and shows how closely the model predicts C_F. (b) Root mean squared error of each compound for model 1, the points above the black line are predicted outside an RMS error of ±2 and all contain no hydrogen bond acceptors.

here was only carried out with a limited number of samples most of which had C_F <5 $e^-/Å^2$ providing a very small representation of compounds that have a C_F >5 $e^-/Å^2$. This may be due to a disproportion number of poorly water soluble drugs having low C_F making it unlikely that less sensitive compounds would have been selected. We have however predicted C_F for another poorly water soluble compound furosemide at 6.2 $e^-/Å^2$ and found this to be close to the subsequently determined experimental value of 7.1 $e^-/Å^2$. In this study we have shown by using only a small sample set of poorly water soluble molecules that C_F can be predicted using information obtained from the chemical structure. This provides the opportunity to save experimental time by screening suitability of compounds for analysis by TEM. However to be more widely applicable to not only poorly water soluble drugs but to other drug molecules, using a larger sample to build the model would be the next step to improve the predictive capabilities. In addition more descriptors shown to be important for compound stability could further improve the model. A more detailed assessment regarding crystal structure, intermolecular bonding present and the reactivity of radicals that form during irradiation, may provide further insight into the mechanisms for individual compounds and a more accurate prediction of C_F. Furthermore the use of the latest generation of detectors and an imaging filer, may allow for better detection of diffraction spots by increasing the signal-to-background ratio. Potentially extending this method of testing the suitability of crystals for TEM analysis, to a broader range of pharmaceuticals than those presented here.

For those compounds that are stable for TEM, this technique offers the possibility to investigate trace amounts of crystalline material that may be present within amorphous formulations during processing or storage. Identifying the sites at which crystallization occurs in these formulations will be the first step to inhibiting it.

Conclusions

In this study, the electron beam stability of 20 different poorly soluble active pharmaceutical ingredients was assessed by measuring the critical fluence for diffraction spots obtained by selected area electron diffraction measurement at the single particle level in TEM. A set of molecular descriptors obtained from the molecular structure or other easy to measure parameters (some of which had been previously shown to have an effect on critical fluence), were then used in principal component analysis in order to determine which were the most influential. It was shown that descriptors relating to the number of aromatic rings, previously believed to be important for the stability of organics in TEM, the number of conjugated carbons and the ratio of conjugated carbons to non-conjugated carbons had the highest positive correlation to critical fluence, confirming that conjugation has the largest impact on compound stability. Descriptors that included hydrogen bond donors, hydrogen bond acceptors and rotatable bonds showed the highest negative correlation. This negative correlation may be due to the removal of hydrogen atoms, via radiolysis rather than knock on damage, causing destabilization of hydrogen bonding networks and loss of crystal structure. The number of halogen atoms and also melting temperature descriptors that had previously been correlated to an increase with critical fluence was shown to have no correlation for this set of compounds.

The molecular descriptors highlighted from PCA were then used to derive several different multiple linear regression models which aimed to provide the most accurate prediction for critical fluence using the fewest number of predictor variables. The best prediction for critical fluence used only three predictor variables, these being ratio of conjugated carbons to non-conjugated carbons, the ratio of hydrogen bond donors to acceptors and the ratio of hydrogen bond acceptors to donors. The three samples which contained no hydrogen bond acceptors gave the largest error when predicting critical fluence; this may be due to the lack of a predictor variable to account for other potential mechanisms of electron beam damage. This predictive model can be used to screen poorly water soluble drugs to establish those that are stable enough for analysis by TEM. TEM then offers the prospect of determining the presence of crystalline material at low levels in ASD at length scales and limits of detection unobtainable by other techniques.

ASSOCIATED CONTENT

Supporting Information. This material is available free of charge via the Internet at http://pubs.acs.org.
Table of compound name and chemical structure used in the study.
Table of molecular descriptors used for PCA.
Scree plot produced from PCA used to select number of principal components.

AUTHOR INFORMATION

Corresponding Author

*sm11msa@leeds.ac.uk

Author Contributions

The experiment work was carried out Mark S'ari. The manuscript was written through contributions of all authors and all authors have given approval to the final version of the manuscript.

ACKNOWLEDGMENT

The authors thank Professor Elaine Martin for her guidance in carrying out and interpreting the PCA and MLR results. The authors gratefully acknowledge financial support by the EPSRC (Award number 1505716) and funding from AstraZeneca is acknowledged.

REFERENCES

(1) Kanaujia, P.; Poovizhi, P.; Ng, W.; Tan, R. Amorphous formulations for dissolution and bioavailability enhancement of poorly soluble APIs. *Powder Technology* **2015**, *285*, 2–15.

(2) Khadka, P.; Ro, J.; Kim, H.; Kim, I.; Kim, J. T.; Kim, H.; Cho, J. M.; Yun, G.; Lee, J. Pharmaceutical particle technologies: An approach to improve drug solubility, dissolution and bioavailability. *Asian Journal of Pharmaceutical Sciences* **2014**, *9*, 304 – 316.

(3) Sareen, S.; Mathew, G.; Joseph, L. Improvement in solubility of poor water-soluble drugs by solid dispersion. *International Journal of Pharmaceutical Investigation* **2012**, *2*, 12 – 17.

(4) Mullin, J. In Crystallization (*Fourth Edition*), fourth edition ed.; Mullin, J., Ed.; Butterworth-Heinemann: Oxford, 2001; pp 181 – 215.

(5) Baird, J. A.; Taylor, L. S. Evaluation of amorphous solid dispersion properties using thermal analysis techniques. *Advanced Drug Delivery Reviews* **2012**, *64*, 396 – 421.

(6) Eddleston, M. D.; Bithell, E. G.; Jones, W. Transmission Electron Microscopy of Pharmaceutical Materials. *Journal of Pharmaceutical Sciences* **2010**, *99*, 4072 – 4083.

(7) Leuner, C.; Dressman, J. Improving drug solubility for oral delivery using solid dispersions. *European Journal of Pharmaceutics and Biopharmaceutics* **2000**, *50*, 47 – 60.

(8) Stenn, K.; Bahr, G. Specimen damage caused by the beam of the transmission electron microscope, a correlative reconsideration. *Journal of Ultrastructure Research 1970*, *31*, 526 – 550.

(9) Egerton, R.; Li, P.; Malac, M. Radiation damage in the TEM and SEM. *Micron* **2004**, *35*, 399 – 409.

(10) Egerton, R. Control of radiation damage in the TEM. *Ultramicroscopy* **2013**, *127*, 100 – 108.

(11) Jones, W.; Thomas, J. M. Applications of electron microscopy to organic solid-state chemistry. *Progress in Solid State Chemistry* **1979**, *12*, 101 – 124.

(12) Henderson, R.; Glaeser, R. M. Quantitative analysis of image contrast in electron micrographs of beam-sensitive crystals. *Ultramicroscopy* **1985**, *16*, 139 – 150.

(13) Hayashida, M.; Kawasaki, T.; Kimura, Y.; Takai. Y. Estimation of suitable condition for observing copper–phthalocyanine crystalline film by transmission electron microscopy. *Nuclear Instruments and Methods in Physics Research B* **2006,** 248 (2), 273-278.

(14) Egerton, R. F. Choice of operating voltage for a transmission electron microscope. *Ultramicroscopy* **2014**, 145, 85-93.

(15) Glaeser, R. M. Limitations to significant information in biological electron microscopy as a result of radiation damage. *Journal of Ultrastructure Research* **1971**, *36*, 466 – 482.

(16) Revol, J. F.; Manley, R. S. J. Lattice imaging in polyethylene single crystals. *Journal of Materials Science Letters* **1986**, *5*, 249–251.

(17) Jones, W. In *Surface and Defect Properties of Solids: Volume 5* ; Roberts, M. W., Thomas, J. M., Eds.; The Royal Society of Chemistry, 1976; Vol. 5; pp 65 – 80.

(18) Kumar, S.; Adams, W. Electron beam damage in high temperature polymers. *Polymer* **1990**, *31*, 15 – 19.

(19) Pan, M.; Crozier, P. Quantitative imaging and diffraction of zeolites using a slow-scan CCD camera. *Ultramicroscopy* **1993**, *52*, 487 – 498.

(20) Pan, Y.; Brown, A.; Brydson, R. Electron Beam Damage Studies on 6-Line Ferrihydrite. *Journal of Physics: Conference Series* **2006**, *26*, 46.

(21) Alexander, P.; Charlesby, A. Energy transfer in macromolecules exposed to ionizing radiations. *Nature* **1954**, *173*, 578–579.

(22) Fryer, J. The effect of dose rate on imaging aromatic organic crystals. *Ultramicroscopy* **1987**, *23*, 321 – 327.

(23) Fryer, J.; McConnell, C.; Zemlin, F.; Dorset, D. Effect of temperature on radiation damage to aromatic organic molecules. *Ultramicroscopy* **1992**, *40*, 163 – 169.

(24) Nurzynska, K.; Booth, J.; Roberts, C. J.; McCabe, J.; Dryden, I.; Fischer, P. M. Long-Term Amorphous Drug Stability Predictions Using Easily Calculated, Predicted, and Measured Parameters. *Molecular Pharmaceutics* **2015**, *12*, 3389–3398.

(25) Egerton, R; Rauf, I. Dose-rate dependence of electron-induced mass loss from organic specimens. *Ultramicroscopy* **1999**, *80*, 247 – 254.

(26) M.Isaacson, In *Physical Aspects of Electron Microscopy and Microbeam Analysis*; Siegel, B., Beaman, D., Eds.; Wiley, 1975.

(27) Clark, W.; Chapman, J.; MacLeod, A.; Ferrier, R. Radiation damage mechanisms in copper phthalocyanine and its chlorinated derivatives. *Ultramicroscopy* **1980**, *5*, 195 – 208.

(28) Schwarz, G. Estimating the Dimension of a Model. *Ann. Statist*. **1978**, *6*, 461–464.

(29) Akaike, H. A new look at the statistical model identification. *IEEE T-AC* **1974**, *19*, 716–723.

(30) Reimer, L.; Spruth, J. Interpretation of the fading of diffraction patterns from organic substances irradiated with 100 keV electrons at 10-300 K. *Ultramicroscopy* **1982**, *10*, 199 – 210.

(31) Wade, R. The temperature dependence of radiation damage in organic and biological materials. *Ultramicroscopy* **1984**, *14*, 265 – 270.

(32) Knapek, E.; Formanek, H.; Lefranc, G.; Dietrich, I. The interpretation of radiation damage measurements with electron diffraction of organic materials at very low temperatures. *Ultramicroscopy* **1984**, *14*, 253 – 263.

(33) Li, P.; Egerton, R. Radiation damage in coronene, rubrene and p-terphenyl, measured for incident electrons of kinetic energy between 100 and 200kev. *Ultramicroscopy* **2004**, *101*, 161 – 172.

(34) Leijten, Z. J. W. A.; Keizer, A. D. A.; de With, G.; Friedrich, H. Quantitative Analysis of Electron Beam Damage in Organic Thin Films. *The Journal of Physical Chemistry C* **2017**, *121*, 10552–10561.

(35) Grubb, D. T. Radiation damage and electron microscopy of organic polymers. *Journal of Materials Science* **1974**, *9*, 1715–1736.
(36) Howitt, D. G.; Thomas, G. Electron damage in organic crystals. *Radiation Effects* **1977**, *34*, 209–215.

(37) Wade, R.; Pelissier, J. The temperature dependence of the electron irradiation resistance of crystalline paraffin. *Ultramicroscopy* **1982**, *10*, 285 – 290.

(38) Siegel, G. Influence of very low temperature on radiation damage of organic crystals irradiated by 100-keV electrons. *Z. Naturforsch* **1972**, *27a*, 325–332.

(39) Koehler, J. S. Diffusion of Lattice Defects in a Stress Field. *Phys. Rev.* **1969**, *181*, 1015–1019.

(40) Wilkens, M.; Rapps, P. Electron diffraction in crystalline specimens containing a high density of lattice defects. I. Development of a statistical theory. *Physica Status Solidi (a)* **1977**, *44*, 173–182.

(41) Ute Kolb, E. M., Tatiana E. Gorelik; Stewart, A. Structural Characterization of Organics Using Manual and Automated Electron Diffraction. *Polymer Reviews* **2010**, *50*, 385–409.

(42) Fryer, J. R. Radiation damage in organic crystalline films. *Ultramicroscopy* **1984**, 14 (3), 277-236.

(43) Yonekura, K.; Maki-Yonekura, S.; Namba, K. Quantitative Comparison of Zero-Loss and Conventional Electron Diffraction from Two-Dimensional and Thin Three-Dimensional Protein Crystals. *Biophysical Journal* **2002**, 82 (5), 2784-2797.

(44) Conroy, M.; Soltis, J. A.; Wittman, R. S.; Smith, F. N.; Chatterjee, S.; Zhang, X.; Ilton, E. S.; Buck, E. C. Importance of interlayer H bonding structure to the stability of layered minerals. *Scientific Reports* **2017**, *7* .

(45) Westbrook, M. L.; Sindelar, R. L.; Fisher, D. L. Radiolytic hydrogen generation from aluminum oxyhydroxide solids: theory and experiment. *Journal of Radioanalytical and Nuclear Chemistry* **2015**, *303*, 81–86.

(46) Ross, M. W.; DeVore, T. C. Desorption of Nitric Acid From Boehmite and Gibbsite. *The Journal of Physical Chemistry A* **2008**, *112*, 6609–6620.

(47) Ingram-Jones, V. J.; Slade, R. C. T.; Davies, T. W.; Southern, J. C.; Salvador, S. Dehydroxylation sequences of gibbsite and boehmite: study of differences between soak and flash calcination and of particle-size effects. *Journal of Materials Chemistry* **1996**, *6*, 73–79.

For Table of Contents Use Only

Towards developing a predictive approach to assessing electron beam instability during Transmission Electron Microscopy of drug molecules

Mark S'ari, Helen Blade, Rik Brydson, Stephen D. Cosgrove, Nicole Hondow, Leslie P. Hughes and Andy Brown